nature COMMUNICATIONS

ARTICLE

Received 8 Nov 2013 | Accepted 18 Jul 2014 | Published 26 Aug 2014

DOI: 10.1038/ncomms5752

# Enhancing 2D growth of organic semiconductor thin films with macroporous structures via a small-molecule heterointerface

Boseok Kang[1,*], Moonjeong Jang[1,2,*], Yoonyoung Chung[3,*], Haena Kim[1], Sang Kyu Kwak[2], Joon Hak Oh[1] & Kilwon Cho[1,3]

The physical structure of an organic solid is strongly affected by the surface of the underlying substrate. Controlling this interface is an important issue to improve device performance in the organic electronics community. Here we report an approach that utilizes an organic heterointerface to improve the crystallinity and control the morphology of an organic thin film. Pentacene is used as an active layer above, and *m*-bis(triphenylsilyl)benzene is used as the bottom layer. Sequential evaporations of these materials result in extraordinary morphology with far fewer grain boundaries and myriad nanometre-sized pores. These peculiar structures are formed by difference in molecular interactions between the organic layers and the substrate surface. The pentacene film exhibits high mobility up to 6.3 $cm^2 V^{-1} s^{-1}$, and the pore-rich structure improves the sensitivity of organic-transistor-based chemical sensors. Our approach opens a new way for the fabrication of nanostructured semiconducting layers towards high-performance organic electronics.

[1] Department of Chemical Engineering, Pohang University of Science and Technology, Pohang 790-784, Korea. [2] School of Energy and Chemical Engineering, Ulsan National Institute of Science and Technology, Ulsan 689-798, Korea. [3] Polymer Research Institute, Pohang University of Science and Technology, Pohang 790-784, Korea. * These authors contributed equally to this work. Correspondence and requests for materials should be addressed to J.H.O. (email: joonhoh@postech.ac.kr) or to K.C. (email: kwcho@postech.ac.kr).

The semiconductor–dielectric interface significantly affects the performance and the reliability of field-effect transistors[1–4]. In organic field-effect transistors (OFETs), especially in a bottom-gate configuration, the surface of the gate dielectric affects the growth and the morphology of the semiconducting layer, which in turn determines how fast charge carriers can move in the channel region[5]. As grain boundaries[6] and dislocations[7] prevent efficient charge transport between adjacent molecules, reducing such disorders in molecular packing has been extensively studied[8–10]. By adding an interfacial layer, such as self-assembled monolayers (SAMs) and polymeric materials, between the semiconductor and the underlying substrate, the interface properties can be controlled effectively for favourable mesoscale/nanoscale ordering of the organic semiconducting layer[5]. It is generally known that the surface of well-ordered SAMs promotes the two-dimensional (2D) growth of vacuum-deposited organic semiconductor thin films and improves the crystallinity; the surface of disordered SAMs is believed to degrade the film quality by reducing the interaction between the surface and admolecules, inducing the three-dimensional growth rather than the 2D growth[11,12].

Here we report that a soft and rubbery organic surface that has a suitable interaction energy with organic admolecules can induce the quasi 2D growth with few nuclei and result in high-quality organic thin films with indistinct grain boundaries. Compared with previous high-quality pentacene grains in the range of few micrometres, our pentacene films exhibit much larger grains and crystalline homogeneity. Furthermore, a high-quality macroporous pentacene thin film is formed by selective adsorption and enhance lateral diffusion on an organic heterointerface. Sequential evaporations of a small-molecule dielectric and pentacene result in high field-effect mobility ($\mu_{FET}$), up to 6.3 $cm^2 V^{-1} s^{-1}$, as well as nanometre-sized pores in the organic layers having vertical orientation with respect to the substrate. We attribute this high $\mu_{FET}$ to the large and continuously connected pentacene grains, and to the clean interface between the two organic layers, which are evaporated without breaking vacuum. The macropores are found to enhance the sensitivity of OFET-based chemical sensors because of the enhanced diffusion of analytes into the active channel region.

## Results

**Material properties and device fabrication**. For the insulating small-molecule organic layer, we employed *m*-bis(triphenylsilyl) benzene (TSB3), as shown in Fig. 1a. This organosilicon compound has a high energy gap of 3.6 eV in a thin film (Supplementary Fig. 1a), due to the electronically isolated phenyl rings. The highest occupied molecular orbital (HOMO) level of TSB3 was estimated to be −7.1 eV by density functional theory (DFT) calculations, which is far lower than that of pentacene (−5.0 eV) (Supplementary Fig. 1b). The HOMO level was also experimentally confirmed by using cyclic voltammetry (Supplementary Fig. 1c). As a result, unfavourable charge transfer between TSB3 and pentacene is minimized during OFET operations. The glass transition temperature ($T_g$) and melting temperature ($T_m$) of TSB3 were estimated to be 33 and 238 °C, respectively (Supplementary Fig. 1d). For the fabrication of OFETs, TSB3 and pentacene molecules were sequentially deposited in a thermal evaporator ($<10^{-6}$ torr) while *n*-octadecyltrimethoxysilane (OTS)-treated $SiO_2$ substrates were heated to 60 °C, which is higher than the $T_g$ of TSB3. The detailed fabrication process is described in the Methods section. The structure of the OFET is schematically illustrated in Fig. 1a. As control devices, another set of pentacene OFETs was also fabricated on OTS-treated $SiO_2$ excluding the evaporation of TSB3.

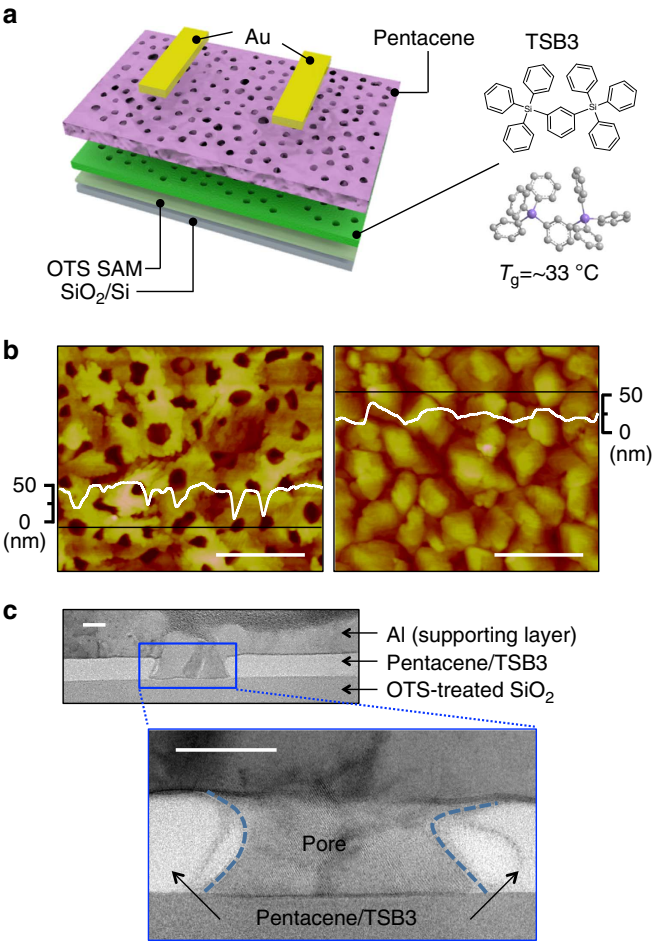


**Figure 1 | Device structure and morphology of organic layers.** (**a**) Device schematic and the molecular structure of TSB3. (**b**) AFM height images of (left) pentacene (45 nm)/TSB3 (15 nm) and (right) pentacene (45 nm) on OTS-treated $SiO_2$. A large number of pores are present in the pentacene/TSB3 film. Scale bars, 1 μm. (**c**) Cross-sectional HRTEM image of pentacene (45 nm)/TSB3 (15 nm) on OTS-treated $SiO_2$. The depth of the pore, also clearly observed in the AFM image of Fig. 1b, is the same as the thickness of the pentacene/TSB3 layers. Scale bars, 50 nm.

**Macroporous pentacene film with indistinct grain boundaries**. We first examined the morphological and the crystalline characteristics of the organic thin films. As shown in the atomic force microscopy (AFM) images of Fig. 1b, the presence of the TSB3 layer drastically alters the morphology of pentacene. In contrast to the small pentacene grains obtained in the absence of TSB3, the pentacene layer with TSB3 is continuously connected with indistinct grain boundaries. Dendritic or faceted grains have been commonly observed from pentacene thin films evaporated on a variety of substrates such as polymers, SAMs and inorganic layers[9]. The extraordinary pentacene morphology on TSB3 indicates that the TSB3 layer significantly affects the growth of the pentacene film. The pores in the pentacene film on TSB3 range in size from 50 to 150 nm, and their depth is found to be similar to the thickness of the organic layers (Fig. 1b). A cross-sectional image of the pores was obtained with high-resolution transmission electron microscopy (HRTEM) in Fig. 1c. The pores are connected to the OTS surface, which confirms that the pore depth corresponds to the combined thickness of the organic layers. It is noteworthy that no grain boundary defects are visible in the cross-sectional HRTEM image within the pentacene layer on TSB3, which is in agreement with the AFM image in Fig. 1b

(detailed cross-sectional HRTEM analysis can be found in Supplementary Fig. 2).

The electrical characteristics of the pentacene OFETs with and without TSB3 were measured in the saturation regime inside a nitrogen-filled glovebox. As shown in Fig. 2a, the pentacene OFETs with TSB3 exhibited higher output currents compared with the pentacene OFETs without TSB3 (Supplementary Fig. 3 for current–voltage curves in logarithmic scale and drain current versus drain–source voltage curves). The pentacene OFETs with TSB3 had an average $\mu_{FET}$ of 5.5 ($\pm$0.7) $cm^2 V^{-1} s^{-1}$, whereas the pentacene OFETs without TSB3 showed an average $\mu_{FET}$ of only 1.5 ($\pm$0.2) $cm^2 V^{-1} s^{-1}$. The $I_{ON}/I_{OFF}$ ratios of both sets of OFETs were $>10^6$, and the threshold voltage values were $-37.5$ ($\pm$0.8) V (with TSB3) and $-33.5$ ($\pm$1.1) V (without TSB3).

A thorough investigation of the pentacene/TSB3 interface is needed to elucidate the remarkably high $\mu_{FET}$ of the pentacene OFETs with TSB3, because charge transport in OFETs occurs in the channel region in the vicinity of the gate dielectric[13]. The morphology of TSB3 is, however, unstable owing to its low $T_g$, so the growth dynamics of pentacene thin films on TSB3 is difficult to study directly. We observed huge clusters of TSB3 after deposition of a 15-nm-thick TSB3 layer on OTS-treated $SiO_2$ (Fig. 2b). Such clusters were also found in pentacene (5 and 10 nm)/TSB3 (15 nm) layers; however, such clustering was not observed when a thick layer of pentacene (>20 nm) was deposited onto the TSB3 film (Fig. 2c–f). We speculate that the TSB3 layer becomes stable in the presence of a thick upper pentacene layer, which suppresses the agglomeration of the bottom TSB3. We performed 2D grazing incidence X-ray diffraction (GIXD) measurements on 5-nm-thick pentacene on TSB3. The 2D GIXD pattern in Fig. 2g indicates that the first few layers of pentacene on TSB3 have a predominant thin-film phase.

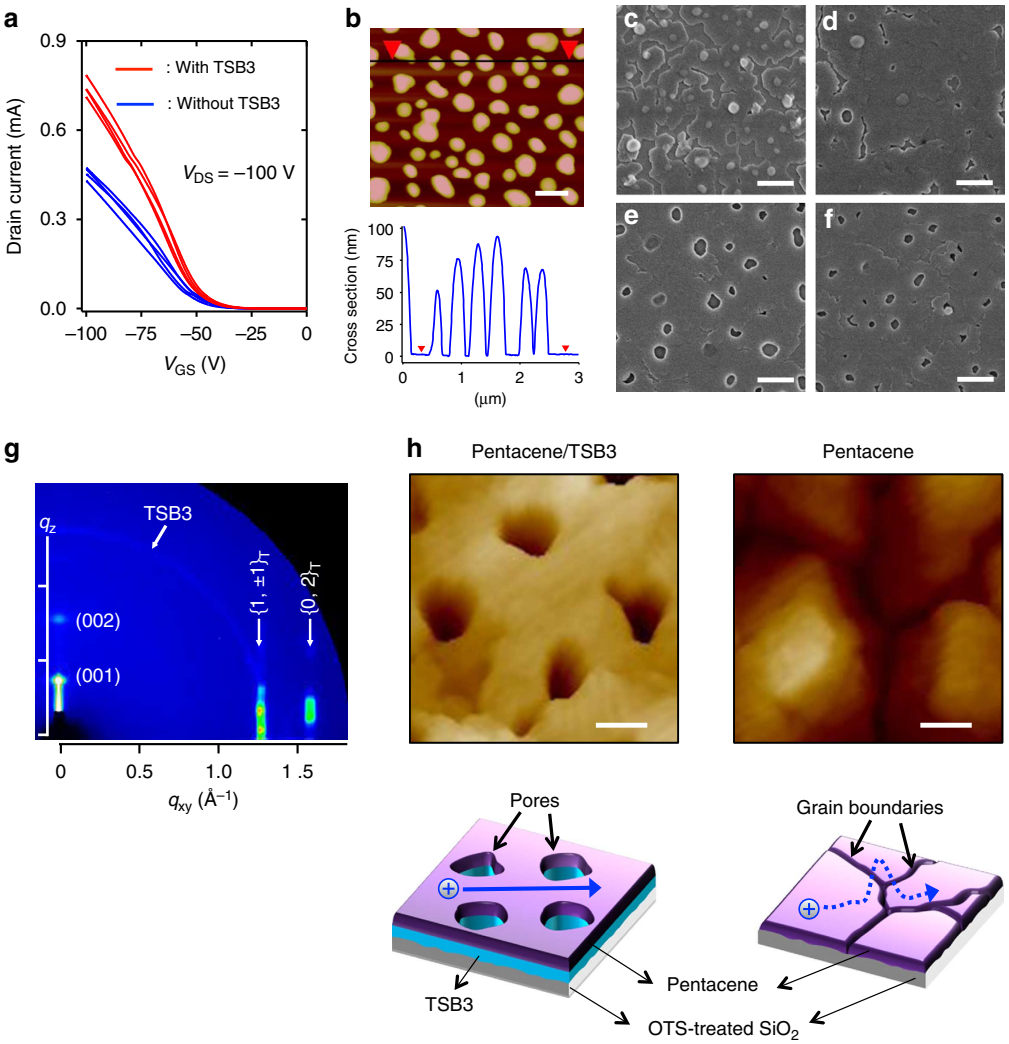


**Figure 2 | Electrical measurement data for the pentacene OFETs and morphological analysis.** (**a**) Current–voltage curves for pentacene OFETs with and without TSB3, measured inside a nitrogen-filled glovebox. Pentacene/TSB3 OFETs: [$\mu_{FET}$ = 5.5 ($\pm$0.7) $cm^2 V^{-1} s^{-1}$, $V_{TH}$ = $-37.5$ ($\pm$0.8) V, $I_{ON}/I_{OFF}$ = 3.7 ($\pm$0.5) $\times 10^6$]; pentacene OFETs: [$\mu_{FET}$ = 1.5 ($\pm$0.2) $cm^2 V^{-1} s^{-1}$, $V_{TH}$ = $-33.5$ ($\pm$1.1) V, $I_{ON}/I_{OFF}$ = 6.9 ($\pm$3.2) $\times 10^6$]. (**b**) AFM height image and cross-sectional profile of a 15-nm-thick TSB3 film on OTS-treated $SiO_2$. When the TSB3 thin film is deposited without a rigid layer on top, the substrate surface is severely dewetted, and the TSB3 film becomes agglomerated. Scale bar, 500 nm. (**c**–**f**) Scanning electron microscope images of pentacene (film thicknesses (**c**) 5, (**d**) 10, (**e**) 20, (**f**) 45 nm)/TSB3 (15 nm) on OTS-treated $SiO_2$. Similar to Fig. 2b, clusters are also found in pentacene (5 and 10 nm)/TSB3 layers. However, such clusters are not observed when a thick layer of pentacene (20 and 45 nm) is deposited onto the TSB3 film. Scale bars, 500 nm. (**g**) 2D GIXD image of pentacene (5 nm)/TSB3 (15 nm) on OTS-treated $SiO_2$. Predominantly the thin-film-phase peaks are present. (**h**) Magnified AFM images of pentacene (45 nm)/TSB3 (15 nm) and pentacene (45 nm) on OTS-treated $SiO_2$, and a schematic diagram of the charge transport inside pentacene layers with and without TSB3. Scale bars, 200 nm.

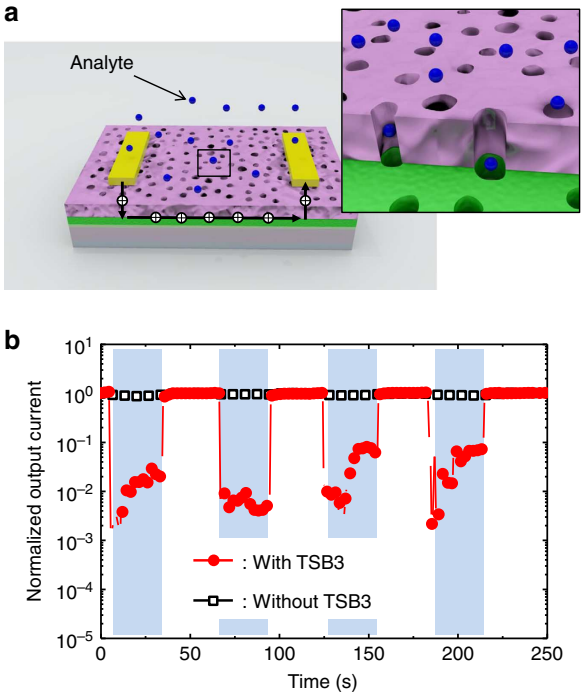


**Figure 3 | OFET-based chemical sensor utilizing the vertical macropores.** (**a**) Schematic diagram of an OFET-based sensor with macroporous layers made of pentacene and TSB3. (**b**) Variation of the output current in the sensor as a function of time. The bias stress effect was compensated by dividing the raw data by the current without the flow of analyte, and the data were normalized to the initial current at $t = 0$. The blue regions indicate the flow of methanol gas (analyte). As clearly shown in the plot, the sensor with TSB3, having vertical macropores, exhibits higher sensitivity than the sensor without TSB3. Both $V_{GS}$ and $V_{DS}$ were fixed at $-100$ V.

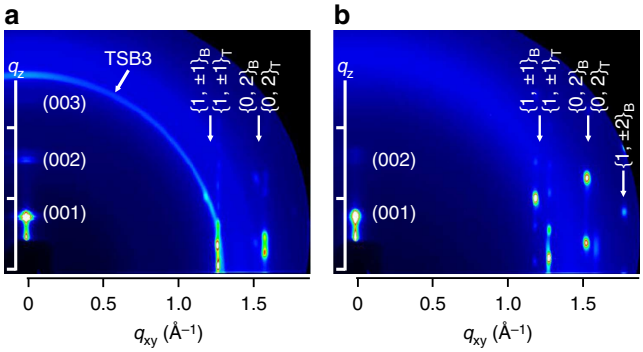


**Figure 4 | GIXD images of the pentacene thin film with and without TSB3.** (**a**) Pentacene (45 nm)/TSB3 (15 nm) on OTS-treated $SiO_2$. The pentacene layer with TSB3 shows dominant thin-film-phase peaks. (**b**) Pentacene (45 nm) on OTS-treated $SiO_2$. The pentacene layer without TSB3 shows dominant bulk-phase peaks.

It is known that the coexistence of different pentacene polymorphs can contribute to an increase in the charge-transfer resistance due to the inter-grain and inter-domain structural mismatches between different crystalline phases[10,14,15]. We attribute the high $\mu_{FET}$ of pentacene OFETs with TSB3 to the structural homogeneity of the first few layers of pentacene, which contain far fewer grain boundaries, as well as to the clean semiconductor (pentacene)/dielectric (TSB3 on OTS-treated $SiO_2$) interface, produced by the sequential evaporation process without breaking vacuum, as illustrated schematically in Fig. 2h.

**Chemical sensors based on macroporous pentacene thin film.** In addition to the typical switching operation in logic circuits, OFETs can be used for sensor devices[16–19]. In general, the output current of OFET-based sensors and detectors is scaled with the amount of target species diffused into the channel region[20]. In OFET-based chemical sensors, the device structure often limits their performance by blocking the efficient diffusion of analytes into the active channel region. Thus, organic semiconducting films with porous structures that facilitate charge transport may be ideal for OFET-based chemical sensors. The vertical macropores in the pentacene/TSB3 layers can improve the sensitivity of OFET-based chemical sensors by enhancing the diffusion of analytes into the channel region. In contrast to previous OFET-based sensors, in which the analytes diffuse into the channel through grain boundaries[20], the macropores provide more efficient and direct pathways, which eventually lead to fast response and high sensitivity to the changes in analyte concentration (Fig. 3a). We monitored the changes in the output current of pentacene OFETs with and without TSB3 while the flow of vapourized methanol was turned on and off sequentially. To confirm that methanol does not swell nor dissolve TSB3, a TSB3 layer was exposed to vapourized methanol, and its morphology was examined by AFM. The exposure of the TSB3 layer to methanol did not affect its physical structure. It is known that methanol molecules typically decrease the channel charge density of p-channel devices due to its electron-donating characteristics[21]. As shown in Fig. 3b, the OFET-based sensor with TSB3 exhibited a significant decrease in the output current when the device was exposed to methanol vapour. In addition, the response and recovery occurred within a few seconds, which demonstrates a remarkably fast and stable performance compared with previous OFET-based sensors[22,23] as well as for other chemical sensors based on conducting polymers[24], carbon nanotubes[25] or inorganic semiconductors[26]. On the other hand, the OFET-based sensors without TSB3 showed much lower sensitivity under the same condition. These results indicate that the macroporous structure induced by TSB3 is highly beneficial to improving the performance of OFET-based sensor devices.

## Discussion

The flat and smooth morphology of pentacene on TSB3 is evidence for the Frank-van der Merwe growth of the pentacene admolecules[3]. In the Frank-van der Merwe growth, admolecules attach preferentially to the substrate surface rather than to the pre-deposited area, which leads to the formation of atomically smooth and fully covered layers[27]. Figure 4 shows 2D GIXD patterns of pentacene thin films with and without TSB3. The (00*l*) reflections in the $q_z$ direction (out-of-plane) indicate that pentacene molecules have stand-up orientation on TSB3. The two intense in-plane reflections, appearing vertically at a given $q_{xy}$, can be indexed to {1, ±1} and {0, 2}, respectively; each reflection index represents two distinct crystalline polymorphs of pentacene thin film, which are referred to as the pseudo-orthorhombic 'thin-film' phase and the triclinic 'bulk' phase[28]. The multiple reflection spots in these vertical 'Bragg-rods' suggest that our pentacene films consist of ordered multi-stacked layers in both vertical and lateral directions[29]. Interestingly, the pentacene film on TSB3 consists predominantly of the thin-film phase, whereas both thin-film and bulk phases are present in the pentacene film without TSB3. Note that the circular pattern at $q_r \approx 1.37$ Å$^{-1}$ in Fig. 4a is due to the underneath TSB3 layer, which is not preferentially oriented on the substrate (Supplementary Fig. 4).

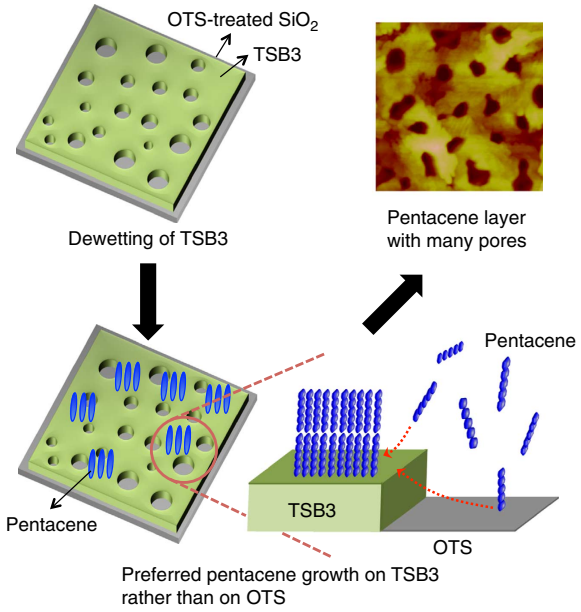


**Figure 5 | Proposed mechanism for the growth of pentacene on TSB3.** In this growth model, the pores in pentacene are expected to form on the exposed OTS surface.

We devise the mechanism in Fig. 5 for the growth of pentacene on TSB3 to explain the indistinct grain boundaries and the formation of the pores. Molecular dynamics (MD) simulations were performed to test our model[30,31]. First, the direct contact between TSB3 and OTS was studied in an attempt to explain the dewetting of TSB3. The interaction energy between TSB3 molecules is more negative, that is, more attractive, than the interaction energy between TSB3 and OTS (Supplementary Fig. 5). This result indicates that agglomeration of TSB3 occurs instead of covering the substrate. The atomically smooth OTS layer with low surface energy may also expedite the dewetting of TSB3, which is already in a rubbery state because the substrate temperature is higher than its $T_g$. Once pentacene is evaporated, it starts to be adsorbed onto the rubbery TSB3 film rather than onto the dewetted OTS area. We calculated the TSB3–pentacene and OTS–pentacene interaction energies with MD simulations. Monolayer, bilayer and trilayer of pentacene were constructed on TSB3 and OTS (Supplementary Fig. 6); the relatively unfavourable interaction (that is, larger positive binding energy) is estimated between pentacene and OTS. This result indicates that the deposition of evaporated pentacene molecules occur preferentially on the TSB3 surface rather than OTS. When the pentacene molecules encounter the dewetted OTS surface, they are captured by the pentacene/TSB3 layers through the van der Waals force. To confirm this selective growth, we simulated the movement of the pentacene molecules by placing them at the boundary between the TSB3 and OTS layers, as shown in Fig. 6. After 50 ps, the pentacene molecules, which straddled at the boundary, have diffused towards the TSB3 layer. Previously, Bao *et al.*[32] estimated the mean travelling distance of pentacene molecules on OTS surfaces using the capture zone model: 0.67 and 1.12 μm for crystalline and amorphous OTS, respectively. Since in our study the size of the pores in the pentacene film with TSB3 ranges from 50 to 150 nm, the pentacene molecules deposited on dewetted OTS have enough time to escape to the pentacene/TSB3 layer. Thus, the large number of macropores in the pentacene thin film on TSB3 is attributed to the dewetting of TSB3 and the preferential growth of pentacene via diffusion onto TSB3 rather than OTS.

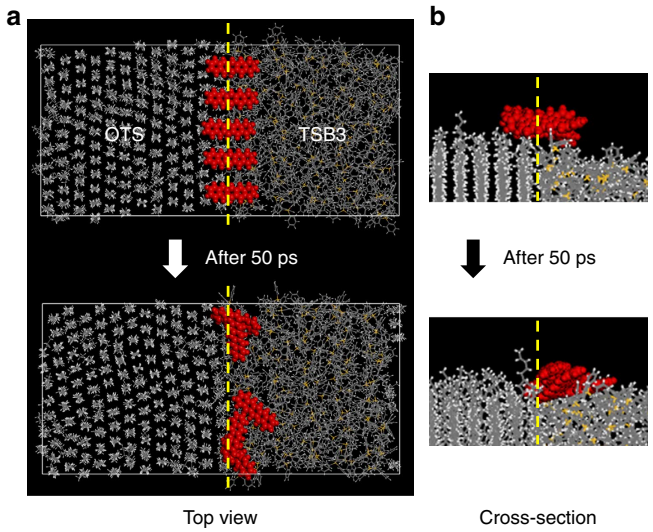


**Figure 6 | Molecular dynamics simulation of pentacene diffusion.** (**a**) Top view and (**b**) cross-sectional snapshots of the molecular dynamics system of pentacene on the interfacial region between TSB3 and OTS. The upper images show the beginning of the simulation. After 50 ps, the pentacene molecules gradually diffuse towards TSB3, which confirms that pentacene has higher attractive interaction with TSB3 than OTS. Yellow dashed lines indicate the boundary between OTS and TSB3.

The high $\mu_{FET}$ of the pentacene OFETs with TSB3 indicates that the macropores in the pentacene layer do not severely affect the charge transport, as depicted in Fig. 2h. During the growth of pentacene, the nucleation density ($N$) in the first seeding layer is known to be related to the ratio between the diffusion constant ($D$) and the deposition rate ($F$) by the following equation: $N \approx F/D$[33]. In our experiment, $N$ is mainly dependent on the $D$ of pentacene adsorbed on the surface, because $F$ remains constant by controlling the evaporation condition. The $D$ value seems to be larger on the TSB3 surface than on the OTS, as inferred from the enlarged crystal domains with indistinct grain boundaries on

the TSB3 layer. The soft and rubbery characteristics of the TSB3 surface facilitate the lateral diffusion of pentacene molecules[32,34]. Similarly, previous studies revealed higher $D$ values for pentacene admolecules on disordered SAMs, which have mobile alkyl chains and soft surface, than on ordered SAMs[11,12]. This enhanced surface diffusion contributes to the self-ordering of pentacene with far fewer grain boundaries in the first seeding layer. Kim *et al.*[35] reported that the surface viscoelasticity of polymer gate dielectrics affects the performance of pentacene transistors; pentacene thin films deposited at substrate temperatures higher than the $T_g$ of the polymer dielectrics had inferior pentacene crystallinity and morphology. In the case of these polymer dielectrics, however, the attractive interactions with pentacene molecules are much stronger than our soft small-molecule dielectric TSB3 (see the MD simulation results in Supplementary Fig. 7). Therefore, the diffusivity of pentacene admolecules is reduced on the polymers, which hinders the growth of high-quality pentacene thin films.

In summary, we investigate the effects of the organic heterointerface between rubbery small-molecule dielectric and pentacene on the performance of OFETs and chemical sensors. TSB3, an organosilicon insulating compound with low $T_g$, significantly changes the morphology of the pentacene thin layer and affects the device performance. Continuously interconnected pentacene grains with far fewer grain boundaries are formed on TSB3, leading to remarkably high $\mu_{FET}$ up to 6.3 $cm^2 V^{-1} s^{-1}$. In addition, a large number of vertical macropores in the organic layers significantly improve the sensitivity of chemical sensors. Our finding demonstrates that organic small-molecule heterointerfaces, enabling a sophisticated control of the growth and morphology in organic thin films, can be utilized to improve the performance of organic electronic devices and to expand their applications.

## Methods

**Device fabrication.** Heavily doped silicon wafers (n-type, $<0.004\,\Omega$ cm) with thermally grown 300-nm-thick $SiO_2$ were used as substrates. The $SiO_2$/Si wafers were cleaned with piranha solution (a mixture of 70 vol% $H_2SO_4$ and 30 vol% $H_2O_2$), followed by ultraviolet-ozone treatment. The surface of the wafers was modified with *n*-OTS SAM.[36] The OTS solution (3 mM in trichloroethylene) was spin-coated at 3,000 r.p.m. for 30 s onto the wafers, and then the samples were kept overnight in a vacuum desiccator with a few drops of $NH_4OH$. The wafers were washed with toluene, acetone and isopropyl alcohol, and dried under nitrogen gas. The contact angle of deionized water on the OTS-treated $SiO_2$ was typically above 110°.

To fabricate the OFETs, TSB3 (15 nm) and pentacene (45 nm) layers were sequentially deposited onto the OTS-treated $SiO_2$/Si substrates in a thermal evaporator without breaking vacuum. The base pressure was below $5.0 \times 10^{-6}$ torr, and the deposition rate was maintained at 0.1–0.2 Å $s^{-1}$. For pentacene OFETs without TSB3, only a pentacene layer (45 nm) was thermally evaporated. During the evaporation, the samples were heated at 60 °C. Gold source/drain electrodes (40 nm) were thermally evaporated through a shadow mask onto the pentacene layer. The source/drain patterns had a channel length ($L$) of 50 μm and a channel width ($W$) of 1,000 μm ($W/L = 20$).

To measure the capacitance of the gate dielectric, TSB3 (15 nm) and gold electrode patterns (40 nm) were deposited sequentially onto OTS-treated $SiO_2$/Si with gold electrode patterns in a single vacuum process.

**Electrical measurement.** The current–voltage characteristics of the OFETs were measured inside a glovebox filled with nitrogen gas using a Keithley 4200-SCS semiconductor parametric analyzer. The field-effect mobility ($\mu_{FET}$) and the threshold voltage ($V_{TH}$) were estimated in the saturation regime ($V_{DS} = -100$ V) with the following equation:[13]

$$I_D = \frac{W}{2L}\mu_{FET}C_g(V_{GS} - V_{TH})^2, \quad (1)$$

where $I_D$ is the drain current, $C_g$ is the capacitance of the gate dielectric and $V_{GS}$ is the gate-source voltage.

In the sensor measurements, methanol vapour was produced by flowing nitrogen gas into a flask filled with liquid methanol. Vapourized methanol then flowed to the sensor device through a 3-mm-wide tube. The end of the tube was installed 5 cm above the surface of the device. While the flow of methanol was on, the gas flow was maintained at 4 s.c.c.m.

The capacitance of the gate dielectric was measured with an Agilent 4284A. Both OTS-$SiO_2$ (300 nm) and TSB3 (15 nm)-OTS-$SiO_2$ (300 nm) samples had almost identical capacitance of 11 nF $cm^{-2}$.

**Morphology characterization.** The surface morphologies were characterized with an AFM (Digital Instruments Multimode) and a scanning electron microscope (Hitachi S-4200).

2D GIXD measurements were performed at the 3C and 9A beamlines of the Pohang Accelerator Laboratory.

Cross-sectional HRTEM images were obtained using a field emission electron microscope (JEOL, JEM-2100F). In the preparation of HRTEM specimens, aluminium (250 nm) and platinum (1.3 μm) layers were sequentially deposited on the samples to protect the organic layers against high-energy gallium ions (acceleration voltage of 30 kV) during the focused-ion-beam milling process (FEI, Helios).

**Material analysis.** The optical and thermal behaviours of TSB3 were measured using a ultraviolet–Visible spectrophotometer (Varian, CARY-5000) and a differential scanning calorimetry (Perkin-Elmer DSC7), respectively.

Cyclic voltammetry was performed using a PowerLab/AD instrument model system. A tetrabutylammonium hexafluorophosphate ($Bu_4NPF_6$) solution in acetonitrile (0.1 M) was used as the electrolyte solution. Three kinds of electrodes were used in the measurements: Ag/AgCl reference electrode, glassy carbon working electrode and platinum counter electrode. The potential of the Ag/AgCl reference electrode was internally calibrated using the ferrocene/ferrocenium redox couple (Fc/Fc+). The energy levels of organic semiconductors were estimated with the equations below:

$$E_{HOMO} = -\left(\left(E_{onset,ox} - E_{1/2(Ferrocene)}\right) + 4.8\right)\,[eV], \quad (2)$$

$$E_{LUMO} = -\left(\left(E_{onset,red} - E_{1/2(Ferrocene)}\right) + 4.8\right)\,[eV]. \quad (3)$$

**DFT calculation.** DFT calculations were performed using the Gaussian 03 package with the Becke, 3-parameter, Lee-Yang-Parr (B3LYP) function and the 6-31G* basis set after optimizing the geometry of TSB3.

**MD simulation.** To interpret the bonding and non-bonding interactions in the atomic systems of interest, the COMPASS (condensed-phase optimized molecular potentials for atomistic simulation studies) force field was employed. The equation for the total interaction energy, $V(R)$, which contains nearly 30 potential energy parameters, has the generic form:

$$V(R) = \left(\sum \nu_{stretching} + \sum \nu_{bending} + \sum \nu_{tortion} + \sum \nu_{deformation}\right)_b + \left(\sum \nu_{Coulomb} + \sum \nu_{van\ der\ Waals} + \sum \nu_{Morse\text{-}dispersion}\right)_{nb}. \quad (4)$$

The first four terms are the energies of bond stretching, angle bending, torsion and deformation, respectively, which mostly are fitted into anharmonic forms. The next three terms are the long-range electrostatic (that is, Coulombic), van der Waals (that is, 9-6 Lennard-Jones) and dispersion (that is, Morse type) interaction energies, respectively. The final term is presented for the simulation of semi-ionic systems. The total interaction energy, $V(R)$, is integrated with respect to time following the Verlet algorithm to provide pairwise momenta between atoms, and the time interval was set to be 1 fs. We performed all-atom MD simulations with the isometric and isothermal ensemble (that is, constant NVT, where $N$ is the number of molecules, $V$ is the volume and $T$ is the temperature) at 60 °C. All systems with interfaces were constructed by adding each constituent system and allowing it to undergo energy minimization with a relaxation period for 10 ps. After each interfacial system was constructed, it was relaxed with the same ensemble for 20–30 ps and run for 100 ps to calculate the binding energies and obtain other results.

## References

1. Podzorov, V. *et al.* Intrinsic charge transport on the surface of organic semiconductors. *Phys. Rev. Lett.* **93,** 086602–086605 (2004).
2. Chua, L. L. *et al.* General observation of n-type field-effect behaviour in organic semiconductors. *Nature* **434,** 194–199 (2005).
3. Heringdorf, F. J. M. Z., Reuter, M. C. & Tromp, R. M. Growth dynamics of pentacene thin films. *Nature* **412,** 517–520 (2001).
4. Klauk, H., Zschieschang, U., Pflaum, J. & Halik, M. Ultralow-power organic complementary circuits. *Nature* **445,** 745–748 (2007).
5. Lee, W. H., Cho, J. H. & Cho, K. Control of mesoscale and nanoscale ordering of organic semiconductors at the gate dielectric/semiconductor interface for organic transistors. *J. Mater. Chem.* **20,** 2549–2561 (2010).

6. Rivnay, J. *et al.* Large modulation of carrier transport by grain-boundary molecular packing and microstructure in organic thin films. *Nat. Mater.* **8,** 952–958 (2009).
7. Nickel, B. *et al.* Dislocation arrangements in pentacene thin films. *Phys. Rev. B* **70,** 125401–125407 (2004).
8. Minemawari, H. *et al.* Inkjet printing of single-crystal films. *Nature* **475,** 364–367 (2011).
9. Ruiz, R. *et al.* Pentacene thin film growth. *Chem. Mater.* **16,** 4497–4508 (2004).
10. Zhang, J., Rabe, J. P. & Koch, N. Grain-boundary evolution in a pentacene monolayer. *Adv. Mater.* **20,** 3254–3257 (2008).
11. Virkar, A. *et al.* The role of OTS density on pentacene and C-60 nucleation, thin Film growth, and transistor performance. *Adv. Funct. Mater.* **19,** 1962–1970 (2009).
12. Lee, H. S. *et al.* Effect of the phase states of self-assembled monolayers on pentacene growth and thin-film transistor characteristics. *J. Am. Chem. Soc.* **130,** 10556–10564 (2008).
13. Horowitz, G. Organic field-effect transistors. *Adv. Mater.* **10,** 365–377 (1998).
14. Street, R. A., Knipp, D. & Volkel, A. R. Hole transport in polycrystalline pentacene transistors. *Appl. Phys. Lett.* **80,** 1658–1660 (2002).
15. Kang, J. H., Da Silva, D., Bredas, J. L. & Zhu, X. Y. Shallow trap states in pentacene thin films from molecular sliding. *Appl. Phys. Lett.* **86,** 152115–152117 (2005).
16. Torsi, L. *et al.* A sensitivity-enhanced field-effect chiral sensor. *Nat. Mater.* **7,** 412–417 (2008).
17. Mannsfeld, S. C. B. *et al.* Highly sensitive flexible pressure sensors with microstructured rubber dielectric layers. *Nat. Mater.* **9,** 859–864 (2010).
18. Gelinck, G. H. *et al.* Flexible active-matrix displays and shift registers based on solution-processed organic transistors. *Nat. Mater.* **3,** 106–110 (2004).
19. Sekitani, T. *et al.* Organic nonvolatile memory transistors for flexible sensor arrays. *Science* **326,** 1516–1519 (2009).
20. Someya, T. *et al.* Chemical and physical sensing by organic field-effect transistors and related devices. *Adv. Mater.* **22,** 3799–3811 (2010).
21. Thompson, T. L. & Yates, J. T. Monitoring hole trapping in photoexcited TiO2(110) using a surface photoreaction. *J. Phys. Chem. B* **109,** 18230–18236 (2005).
22. Zhu, Z. T., Mason, J. T., Dieckmann, R. & Malliaras, G. G. Humidity sensors based on pentacene thin-film transistors. *Appl. Phys. Lett.* **81,** 4643–4645 (2002).
23. Li, L. Q. *et al.* High performance field-effect ammonia sensors based on a structured ultrathin organic semiconductor film. *Adv. Mater.* **25,** 3419–3425 (2013).
24. Geng, L. *et al.* Characterization and gas sensitivity study of polyaniline/$SnO_2$ hybrid material prepared by hydrothermal route. *Sens. Actuators B* **120,** 568–572 (2007).
25. Snow, E. S. *et al.* Chemical detection with a single-walled carbon nanotube capacitor. *Science* **307,** 1942–1945 (2005).
26. Jia, Y. *et al.* Preparation of porous Tin oxide nanotubes using carbon nanotubes as templates and their gas-sensing properties. *J. Phys. Chem. C* **113,** 9581–9587 (2009).
27. Cheng, H. L. *et al.* Thickness-dependent structural evolutions and growth models in relation to carrier transport properties in polycrystalline pentacene thin films. *Adv. Funct. Mater.* **17,** 3639–3649 (2007).
28. Drummy, L. F. & Martin, D. C. Thickness-driven orthorhombic to triclinic phase transformation in pentacene thin films. *Adv. Mater.* **17,** 903–907 (2005).
29. Yang, H. C. *et al.* Conducting AFM and 2D GIXD studies on pentacene thin films. *J. Am. Chem. Soc.* **127,** 11542–11543 (2005).
30. Allen, M. P. & Tildesley, D. J. *Computer Simulation of Liquids* (Oxford Univ. Press, 1987).
31. Frenkel, D. & Smith, B. *Understanding Molecular Simulation: From Algorithms to Applications* (Academic Press, 2002).
32. Virkar, A. A., Mannsfeld, S. C. B. & Bao, Z. N. Energetics and stability of pentacene thin films on amorphous and crystalline octadecylsilane modified surfaces. *J. Mater. Chem.* **20,** 2664–2671 (2010).
33. Ruiz, R. *et al.* Dynamic scaling, island size distribution, and morphology in the aggregation regime of submonolayer pentacene films. *Phys. Rev. Lett.* **91,** 136102–136105 (2003).
34. Kim, D. H. *et al.* Tunable crystal nanostructures of pentacene thin films on gate dielectrics possessing surface-order control. *Adv. Funct. Mater.* **18,** 1363–1370 (2008).
35. Kim, C., Facchetti, A. & Marks, T. J. Polymer gate dielectric surface viscoelasticity modulates pentacene transistor performance. *Science* **318,** 76–80 (2007).
36. Ito, Y. *et al.* Crystalline ultrasmooth self-assembled monolayers of alkylsilanes for organic field-effect transistors. *J. Am. Chem. Soc.* **131,** 9396–9404 (2009).


## Acknowledgements

This work was supported by the Center for Advanced Soft Electronics under the Global Frontier Research Program (2011-0031628 and 2013M3A6A5073175) of the Ministry of Science, ICT and Future Planning and the Basic Science Research Program (NRF-2013R1A1A2012046) through the National Research Foundation of Korea funded by the Ministry of Education. We thank J. Shin, Dr C. Shim, Dr H. G. Kim and Dr N.-S. Lee for discussion, cyclic voltammetry, DFT calculations and HRTEM measurements.

## Author contributions

Y.C., J.H.O. and K.C. conceived the idea and directed the research project. B.K. analysed the morphology and crystallinity of organic thin films. M.J. fabricated all the samples and measured electrical characteristics of organic transistors and chemical sensors. S.K.K. conducted molecular dynamics simulations. H.K. carried out scanning electron microscopy on the surface of organic thin films. All authors discussed the results and commented on the manuscript.

## Additional information

**Supplementary Information** accompanies this paper at http://www.nature.com/naturecommunications

**Competing financial interests:** The authors declare no competing financial interests.

**Reprints and permissions** information is available online at http://npg.nature.com/reprintsandpermissions/

**How to cite this article**: Kang, B. *et al.* Enhancing 2D growth of organic semiconductor thin films with macroporous structures via a small-molecule heterointerface. *Nat. Commun.* 5:4752 doi: 10.1038/5752 (2014).